mater.scichina.com link.springer.com Published online 26 December 2023 | https://doi.org/10.1007/s40843-023-2676-y

SPECIAL ISSUE: Advanced Energy Catalytic Materials

Tuning molecular electrophilicity on Cu catalysts to steer CO_2 electroreduction selectivity

Xianlong Zhou[1,3†], Jieqiong Shan[1†], Min Zheng[1†], Huan Li[1], Bao Yu Xia[2*] and Yao Zheng[1*]

ABSTRACT **Cu is the only transition metal that can achieve electrochemical CO_2 reduction (CRR) with the generation of hydrocarbons and oxygenates. However, it is still challenging to regulate CRR selectivity in a broad product distribution on Cu. Here, we selected a series of molecules with varying electrophilicity to modify Cu catalysts that achieve a high CRR selectivity towards either CH_4 or C_2H_4. Theoretical analysis shows that molecular electrophilicity determines catalyst's proton availability, which promotes or inhibits the critical proton-coupled electron transfer (PCET) process in CRR. Consequently, the molecule with low electrophilicity (e.g., 1,2-bis(4-pyridyl)ethane) can facilitate proton transfer to hydrogenate $^*CO$ intermediates to generate CH_4 with a Faradaic efficiency (FE) of 58.2%, while the molecule with high electrophilicity (e.g., *trans*-1,2-bis(4-pyridyl)ethylene) can build stronger hydrogen bonds to stabilize $^*CO$ for further dimerization, realizing an FE of 65.9% for C_2H_4. The combination of theoretical computation and *in situ* spectroscopic characterizations reveal that using molecular electrophilicity can tune catalyst's proton availability, thereby altering its CRR pathway of either $^*CO$ hydrogenation or $^*CO$–$^*CO$ dimerization. This work provides new understanding of CRR selectivity by tuning the PCET process instead of materials engineering.**

Keywords: molecular electrophilicity, Cu catalysts, proton transfer, CO_2 electroreduction, C1/C2 selectivity

INTRODUCTION

Electrochemical CO_2 reduction (CRR) in aqueous solutions can not only store renewable electricity obtained from intermittent solar or wind energy but also convert CO_2 into value-added chemicals or fuels [1–4]. Because Cu binds to CRR intermediates *CO neither too weakly nor too strongly, it is the only transition metal to deeply convert CO_2 to CH_4, C_2H_4 and C_2H_5OH [5,6]. Unfortunately, this unique physicochemical property of Cu also results in poor product selectivity [7–9]. Various strategies, including alloying [10], oxide derivation [11], and surface modification [12–14], have been developed to engineer Cu for the generation of desired products. In general, these Cu-based catalysts exhibit a high selectivity for one product, such as CO, CH_4 or C_2H_4 [15,16]. For example, Ma *et al.* [17] reported Cu(OH)X (X = F, Cl, Br, I) derived Cu with the highest Faradaic efficiency (FE) of 65.0% for C_2H_4. However, these catalysts display a low selectivity for CH_4. Likewise, although Cu-Au alloy can achieve a high CH_4 FE of 56.0%, a high selectivity for C_2H_4 cannot be obtained on this catalyst family [18]. Therefore, it remains to be a great challenge to tune CRR in a broad product distribution with a high selectivity for one specific product.

It has been confirmed that *CO–*CO coupling is the rate-determining step of C_2H_4 generation, while that of CH_4 generation is the hydrogenation of *CO to *CHO [19–21]. For example, Li *et al.* [22] utilized a series of N-substituted pyridinium additives to stabilize the atop-bound *CO intermediate, thereby realizing a high FE for C_2H_4. Chen *et al.* [23] promoted water splitting to supply high concentration of active protons and achieved a high CO_2-to-CH_4 selectivity. Based on those findings, we hypothesize that stabilizing *CO intermediate with poor proton transfer on Cu surface can promote *CO dimerization to C_2H_4, while a facile proton transfer can directly hydrogenate *CO to CH_4 (Fig. 1a). These two proton-coupled electron transfer (PCET) processes are critical steps to steer the reaction pathway towards desired products. The PCET process has been widely studied in homogeneous catalysis but not yet in heterogeneous CRR [24,25]. Metal-organic frameworks (MOFs), composed of metal nodes and organic linkers, provide a great platform for tuning the coordination environment of metal active centers to optimize the adsorption of *CO [26,27]. More importantly, linker's electrophilicity affects the electrocatalyst's proton availability, which promotes or inhibits the PCET process of either hydrogenation or dimerization. Therefore, different from electronic structure engineering in conventional Cu catalysts, it provides an alternative and insightful way to steer the CRR selectivity [5,28].

As a proof-of-concept, here we employed a class of bipyridyl molecules (1,2-bis(4-pyridyl)ethane (bpa), 1,2-bis(4-pyridyl)-benzene (dpb), 4,4′-bipyridine (bpy) and *trans*-1,2-bis(4-pyridyl)ethylene (bpe)) as linkers with different electrophilicity

[1] School of Chemical Engineering and Advanced Materials, The University of Adelaide, Adelaide, SA 5005, Australia
[2] Key Laboratory of Material Chemistry for Energy Conversion and Storage (Ministry of Education), Hubei Key Laboratory of Material Chemistry and Service Failure; National Laboratory for Optoelectronics, School of Chemistry and Chemical Engineering, Huazhong University of Science and Technology, Wuhan 430074, China
[3] Jiangsu Co-Innovation Centre of Efficient Processing and Utilization of Forest Resources, College of Chemical Engineering, Nanjing Forestry University, Nanjing 210037, China
† These authors contributed equally to this work.
* Corresponding authors (emails: byxia@hust.edu.cn (Xia BY); yao.zheng01@adelaide.edu.au (Zheng Y))

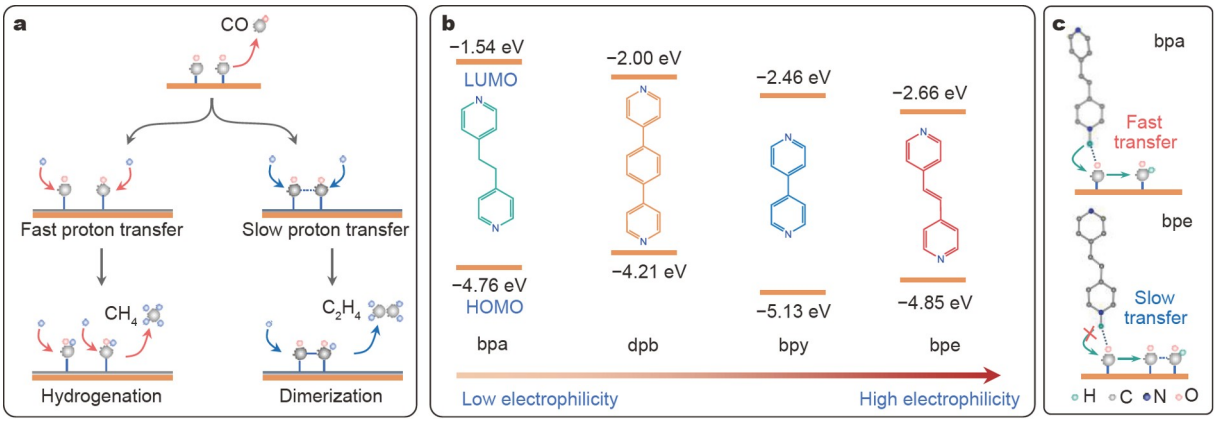

Figure 1 (a) Schematic illustration of PCET processes: hydrogeneration (left) and dimerization (right). (b) Energy levels of N 2p in each molecule. (c) Schematic illustration of proton transfer processes from organic molecules with different electrophilicity: fast (top) and slow (bottom) transfers.

to steer Cu-MOFs' CRR selectivity. Density functional theory (DFT) calculations coupled with *in situ* attenuated total reflectance infrared (ATR-IR) and Raman spectroscopy confirm that the electrophilicity of linker can alter the catalyst's proton availability in PCET reactions. Catalyst with a low-electrophilicity linker exhibits fast proton transfer to *CO, which promotes its protonation to lead to a high FE of 58.2% for CH_4. By contrast, a high-electrophilicity linker can stabilize *CO and favor its C–C coupling step, resulting in a high FE of 65.9% for C_2H_4.

EXPERIMENTAL SECTION

Synthesis of Cu-MOFs

CuCl powder (0.25 g) was dispersed in 25 mL of acetonitrile with sonication for 5 min, and 2.5 mmol of organic linker (bpa, dpb, bpy and bpe) was dissolved in 5 mL of acetonitrile with 10 min sonication. Then, the solution with organic linker was added into the solution with CuCl. Following magnetic stirring for 60 min, the precipitate was washed respectively with acetonitrile and deionized water thrice. All samples were obtained following freeze-drying for 24 h.

Materials characterization

The phase and structure of the as-synthesized samples were analyzed by a Philips PW-1830 X-ray diffractometer (XRD) using Cu Kα radiation (λ = 1.5406 Å, scan rate = 5° min^{-1}). Scanning electronic microscopy (SEM) images and transmission electronic microscopy (TEM) images were collected on a Hitachi New Generation SU8010 SEM and a JOEL 2100 TEM, respectively. X-ray photoelectron spectroscopy (XPS) measurements were conducted on AXIS-ULTRA DLD-600W XPS (mono Al Kα 1486.6 eV) and recorded by the hemispherical analyser with a step-size of 0.05 eV. Fourier-transform infrared (FTIR) spectra were collected on a Nicolet 6700 spectrometer. Thermogravimetric analysis (TGA) profiles were obtained from a TGA/SETARAM thermogravimetric analyzer from 25 to 600°C with a heating rate of 10°C min^{-1} in air flow. The isotope-labelled experiments were carried out using $^{13}CO_2$, and the products were analyzed using gas chromatography-mass spectrometry (7890B and 5977B, Aglient). The extended X-ray absorption fine structure (EXAFS) measurements were carried out on the sample at 21A X-ray nanodiffraction beamline of Taiwan Photon Source (TPS), Synchrotron Radiation Research Centre. This beamline adopted a 4-bounce channel-cut Si (111) monochromator for mono-beam X-ray nanodiffraction and X-ray absorption spectroscopy. The end-station was equipped with three ionization chambers and Lytle/SDD detector after the focusing position of the KB mirror for transmission and fluorescence mode X-ray absorption spectroscopy.

Activity and selectivity measurement

The CRR catalytic activity of different samples was investigated by a commercial flow cell (Gaossunion) in 1 mol L^{-1} KOH solution. The volumes of the anode and cathode chamber electrolyte were both 15 mL. To prepare the working electrode, 25 mg of catalyst was dispersed by sonication in 2.85 mL of isopropanol and 150 μL of 5 wt% of Nafion for 60 min. Next, the inks were airbrushed onto a gas diffusion layer (GDL, Sigracet 29 BC) as the cathode electrode (3 cm × 1 cm, loading mass: 1.0 mg cm^{-2}). The reference and counter electrodes were Ag/AgCl (3.0 mol L^{-1} KCl) and Pt foil (3 cm × 1 cm; 1 mm thickness) connected to a potentiostat (Gamry Interface 3000), respectively. An anion exchange membrane (FAB-PK-130) (Fuel Cell Store) was sandwiched between the two polytetrafluoroethylene sheets to separate the chambers. In addition, 1 mol L^{-1} KOH was circulated around the cathode and the anode at a flow rate of 10.0 mL min^{-1} during the CRR. During this process and then testing, CO_2 was continuously purged at a rate of 20 mL min^{-1}. The gas products were self-injected into a gas chromatograph (Shimadzu GC-2014) equipped with TCD and methanizer/FID detectors. Liquid products were analyzed by H^1 nuclear magnetic resonance spectroscopy (NMR, 400 MHz, Bruker). Dimethylsulfoxide (DMSO) as known internal standards was utilized to obtain a calibration curve to quantifying the liquid products. The resistance of 1.9 Ω had been used to calculate the *iR*-correction. The electrical double layer capacitances (C_{dl}) of samples were used to computer the electrochemical active area of the samples after CRR, which was obtained from CV plots in a small potential range of −0.6 to −0.7 V (*vs.* Ag/AgCl).

XPS and XRD analyses of samples after CRR

We identified the Cu valence state of solid solution and the

phase of catalysts after CRR by XPS analysis or XRD. When we completed the CRR test, the electrode was washed by deionized water and ethanol thrice. The sample after CRR was obtained after vacuum drying for 12 h. Then, we could identify the Cu valent state or the phase of the sample after CRR.

In situ ATR-IR spectroscopy

It was conducted by using a Thermo-Fisher Nicolet iS20 equipped with a liquid nitrogen-cooled HgCdTe (MCT) detector using a VeeMax III ATR accessory (Pike Technologies). A germanium prism (60°, PIKE Technologies) was mounted in a PIKE electrochemical three-electrode cell with a platinum-wire counter electrode and an Ag/AgCl reference electrode (Pine Research). All ATR-IR measurements were acquired by averaging 64 scans at a spectral resolution of 4 cm^{-1}. Electrocatalyst ink was prepared by dispersing catalyst powder (10 mg) in a solution containing isopropanol (1.5 mL) and 5 wt% Nafion solution (50 μL) followed by ultrasonication for 60 min. Then, 50 μL of the catalyst ink was dropped onto the prism and left to dry slowly. The electrolyte was 0.1 mol L^{-1} $KHCO_3$, which was constantly purged with CO_2 during the experiment. A CHI 760E electrochemical workstation (CH Instruments, USA) was connected for chronoamperometric tests from −0.6 to −2.1 V *vs.* Ag/AgCl stepwise. Meanwhile, the spectra under open circuit potential (OCP) were recorded for comparison.

In situ Raman spectroscopy

In situ Raman testing was recorded on a HORIBA LabRAM HR Evolution Raman spectrometer (laser wavelength = 532 nm). For each measurement, the Raman spectrum was collected by two acquisitions (20 s per acquisition). The tests were carried out using a screen-printed chip electrode from Pine Research Instrumentation. The electrocatalyst ink was prepared by dispersing catalyst powder (5 mg) in a solution containing isopropanol (0.75 mL) and 5 wt% Nafion solution (25 μL) followed by ultrasonication for 60 min. Ten microliters of the ink gel were added to the printed electrode before dried at room temperature. The electrolyte was CO_2-saturated 0.1 mol L^{-1} $KHCO_3$.

All calculations in this work were carried out using DFT method as implemented in the Vienna *Ab initio* Simulation Package code. The electronic exchange-correlation energy was modeled using the Perdew–Burke–Ernzerhof (PBE) functional within the generalized gradient approximation (GGA) [29]. The projector augmented wave (PAW) method was used to describe the ionic cores. For the plane-wave expansion, a 450-eV kinetic energy cut-off was used after testing a series of different cut-off energies. A Monkhorst–Pack 2 × 4× 2 *k*-point grid was used to sample the Brillouin zone. The convergence criterion for the electronic structure iteration was set to be 10^{-4} eV, and that for

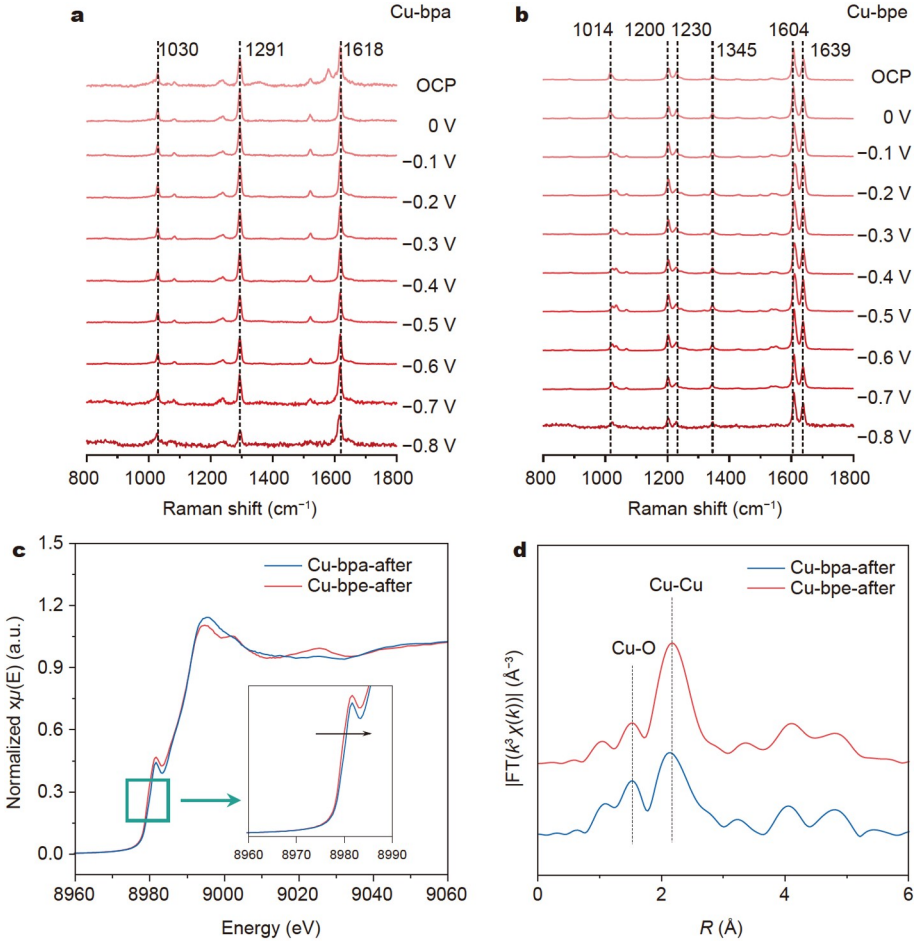

Figure 2 (a, b) *In situ* Raman spectra of Cu-bpa and Cu-bpy collected under different potentials. All potentials are *versus* reversible hydrogen electrode (RHE). (c) Cu K-edge XANES spectra and (d) Fourier transformed Cu K-edge EXAFS spectra of Cu-bpa-after and Cu-bpe-after.

geometry optimizations was set to be 0.01 eV Å^{-1} on force. A Gaussian smearing of 0.1 eV was applied during the geometry optimization for the total energy computations.

RESULTS AND DISCUSSION

Effect of molecular electrophilicity on proton transfer

Cu-based MOFs were synthesized with CuCl and bipyridyl molecules in acetonitrile. Cu-bpy was firstly investigated as its structure has been identified by Yaghi and Li [30]. As illustrated in Fig. S1, two Cu atoms are bridged with two chlorine ligands, and each atom is coordinated to two bpy linkers to form a slightly distorted tetrahedron. The power XRD pattern of Cu-bpy matches well with that of the simulated one (Fig. S2). To investigate the effect of linker's electrophilicity on Cu-MOFs, we chose four linkers (bpa, dpb, bpy and bpe) with two identical pyridyl groups but distinct carbon–carbon linking structures. Since molecule's electrophilicity is relative to its lowest unoccupied molecular orbital (LUMO) position [31], we first used DFT to calculate the projected density of states of N 2p orbitals (N_{2p}) in different linkers (Fig. S3). It is revealed that the electrophilicity of four linkers increases in sequence from bpa to bpe (Fig. 1b). As a result, pyridine (Py) in the linker could be initially protonated to form pyridinium ions (PyH*) intermediate during the electrochemical reaction [32], in which H* can participate in the PCET process [33]. Therefore, the proton availability of these Cu-MOFs is a critical factor in determining the PCET process. Based on the classical Brønsted–Lowry acid–base theory, the proton availability of PyH* depends on the molecule's electrophilicity (Fig. 1c). If the electrophilicity is low, the proton can be easily transferred to the *CO intermediate, favoring its hydrogenation (top). On the contrary, the molecule with high electrophilicity cannot implement this transfer, thereby promoting the dimerization step (bottom). Based on this theoretical analysis, we then synthesized the other three Cu-MOFs (Fig. S4, linker = dpb, bpy and bpe) with the same morphology (Fig. S5). XPS analyses demonstrate that there are two Cu species of Cu^{1+} and Cu^{2+} in Cu-MOFs (Fig. S6) [34]. It is worth noting that a decreased percentage of Cu^{1+} in Cu-MOFs can be observed with the increase of electrophilicity of linker. This is because the linker with high electrophilicity facilitates electronic transfer from metal to pyridine-N and results in the formation of Cu^{2+} [31]. FTIR spectroscopy further indicates that the character peak of C=N bond in bipyridyl molecules decreases from 1614 to 1603 cm^{-1} with the decreased linker electrophilicity due to the electron transfer from metal atoms to organic molecules (Fig. S7).

Characterization of Cu-based MOFs after CRR

It has been known that Cu-based MOFs as CRR catalysts always undergo a structural reconstruction, resulting in the reduction of Cu^{2+} or Cu^{1+} to Cu^0 [35–37]. We employed a set of *in situ* and *ex situ* characterizations to investigate the structure of Cu-MOFs after CRR. The XRD and XPS results prove that Cu-MOFs samples have been electrochemically reduced to stable Cu^0 during CRR operation (Figs S8 and S9). SEM images show that the initial nanosheets have been destroyed during the CRR operation with the formation of nanoparticles and organic materials (Fig. S10). TEM images further confirm that the morphology and size of Cu nanoparticles in derived catalysts are

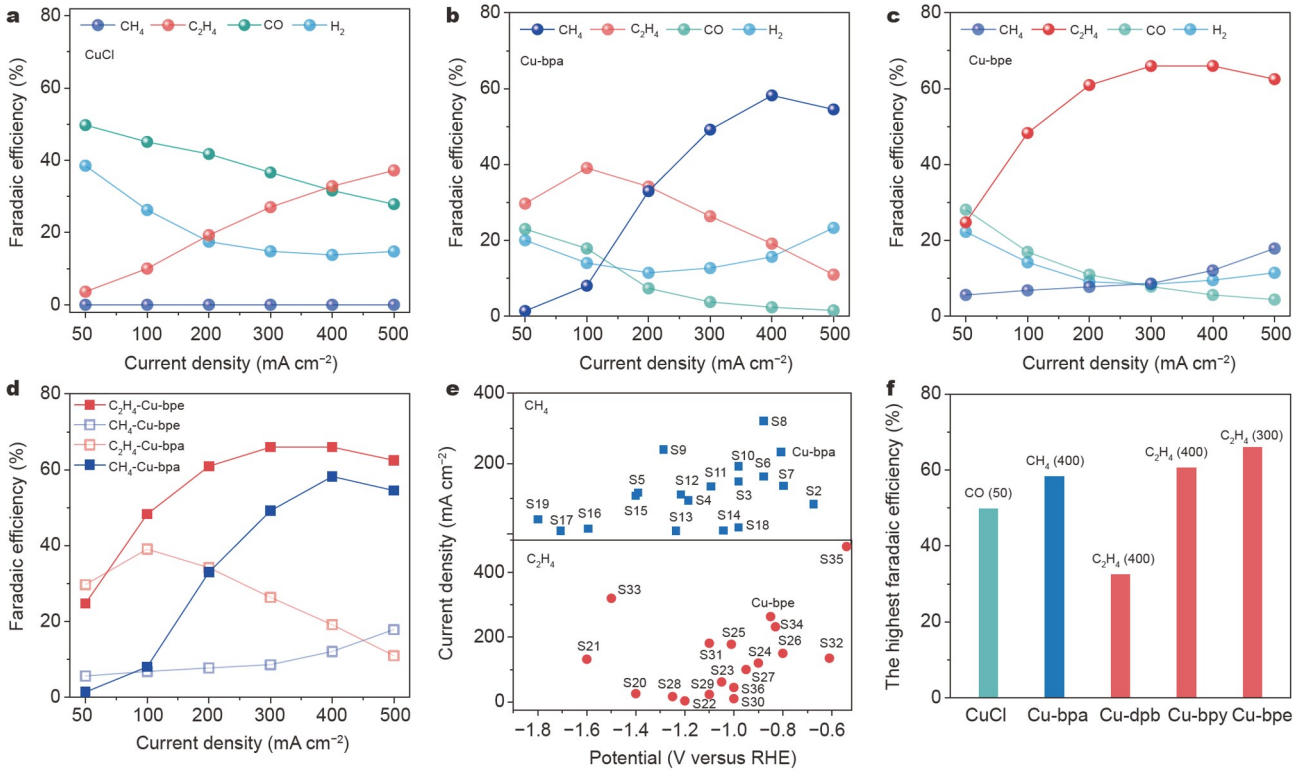

Figure 3 CRR performances of various samples at different current densities. (a–c) FEs for CRR products on various samples; (d) $FE_{C_2H_4}$ and FE_{CH_4} for Cu-bpa and Cu-bpe; (e) FE_{CH_4} of Cu-bpa and $FE_{C_2H_4}$ of Cu-bpe in comparison with other reported Cu-based catalysts after *iR* correction (Tables S3 and S4); (f) their highest FE of distinct CRR products at 50, 400, 400, 500, and 300 mA cm^{-2}, respectively.

same (Fig. S11). *In situ* Raman was used to detect the linkers on the surface of the MOFs-derived Cu under different reaction potentials (Fig. 2a, b, and Fig. S12). The characteristic peaks of organic molecules remain stable under potentials and, more importantly, are consistent with that of pure linkers (Table S1), suggesting that all the linkers steadily adsorb on the surface of Cu catalysts during CRR operations. Cu X-ray absorption near edge structure (XANES) spectra display that Cu species in Cu-bpa exhibit an oxidation state close to that of Cu-bpe after the CRR (samples are defined as Cu-bpa-after and Cu-bpe-after) (Fig. 2c). In the *R*-space EXAFS spectra (Fig. 2d), Cu-bpa-after has a similar Cu–O and Cu–Cu peaks to that of Cu-bpe-after, suggesting that linker's electrophilicity has no effects on the coordination environment of Cu nanoparticles derived from MOFs. Moreover, we also confirmed that the Cu mass percentage and the electroactive surface areas in the derived Cu nanoparticles are similar (Figs S13, S14, and Table S2). Therefore, we conclude that Cu-MOFs samples have been reduced to stable Cu metals coated with linkers after CRR (Fig. S15) and more importantly, the Cu structure effects on the CRR selectivity, for example particle size, morphology, crystallinity, distribution, and chemical composition.

Evaluation of CRR activity

The CRR catalytic performances of the traditional CuCl and Cu-based MOFs were investigated in 1 mol L^{-1} KOH solution by using a flow cell (Figs S16–S19). As shown in Fig. 3a, there is no dominant CRR product for CuCl, which is similar with widely reported oxide-derived Cu [38]. When the linker with lower electrophilicity (e.g., bpa) was introduced, Cu exhibited a strikingly different CRR performance with that of CuCl (Fig. 3b). At large current densities (>200 mA cm^{-2}), the FEs for CH_4 are significantly higher than those of C_2H_4, and a maximum FE_{CH4} of 58.2% can be achieved at 400 mA cm^{-2}. With the catalyst containing high-electrophilicity linkers (e.g., Cu-bpe), high FEs for C_2H_4 up to 65.9% can be achieved at 300 mA cm^{-2} (Fig. 3c). For Cu-dpb, its electrophilicity locates between Cu-bpa and Cu-bpy, and the hydrocarbon product is a mixture of CH_4 and C_2H_4 (Figs S20 and S21). Therefore, we can conclude that the linker with low electrophilicity favors the CH_4 formation, whereas the linker with high electrophilicity benefits the C_2H_4 generation (Fig. 3d). It should be noted that Cu-bpa and Cu-bpe display higher current densities for CH_4 and C_2H_4, respectively, than most of previously reported Cu-based catalysts at a low overpotential zone (Fig. 3e). Importantly, with our Cu-MOF catalysts, the CRR products can be tuned in a wide distribution, whilst a high FE for one specific product (CH_4 or C_2H_4) can be achieved simultaneously (Fig. 3f). We further used $^{13}CO_2$ isotope labeling to prove that the CRR products were resulted from CO_2 reduction rather than carbon containing linkers' decomposition (Fig. S22). In addition, we found that this surface modification of Cu with linkers derived from MOFs can achieve a higher C–C coupling efficiency than that of a physical mixture of commercial Cu nanoparticles and linkers (Fig. S23), further suggesting the importance of *in situ* formed MOF-derived Cu coated with linkers.

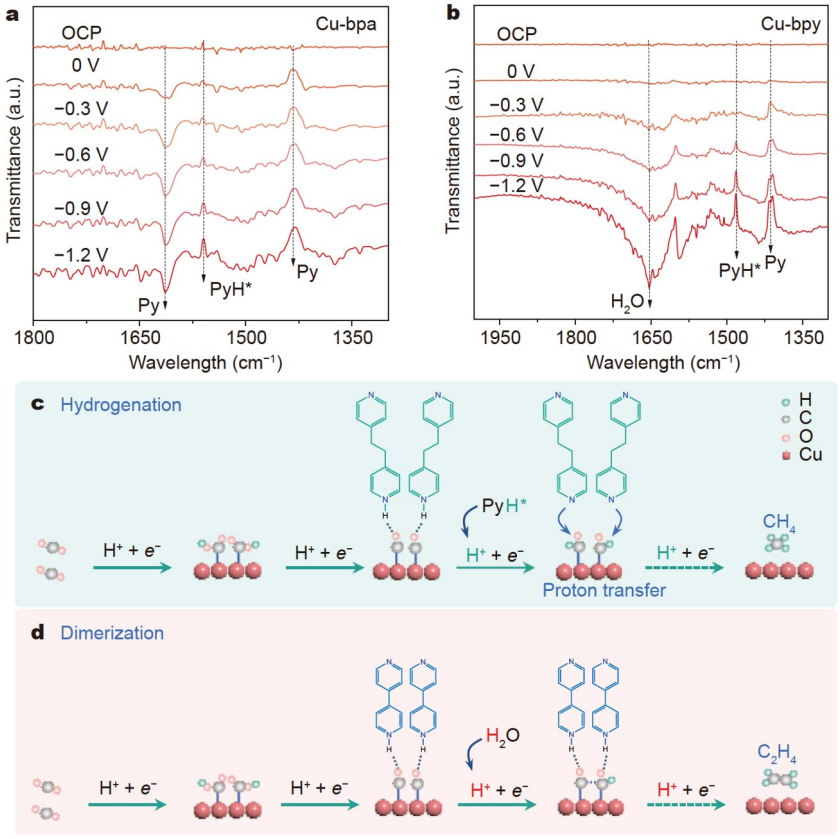

Figure 4 *In situ* ATR-IR spectra to detect proton source and schematic illustration of the formation of CH_4 and C_2H_4. (a, b) *In situ* ATR-IR spectra on Cu-bpa and Cu-bpy under different potentials of CRR. All potentials are *versus* RHE. (c, d) Schematic illustration for the dehydrogenation of PyH* on Cu-bpa and Cu-bpy.

In situ characterization of proton source

To elucidate the distinct selectivity of four samples, we employed *in situ* ATR-IR spectroscopy to analyze the surface structure of catalysts over the CRR process. Firstly, compared with Cu-bpy, a negative peak at 1613 cm^{-1} and a positive peak at 1431 cm^{-1} are observed in Cu-bpa (Fig. 4a), which belong to Py in the bpa linker. The peak at 1560 cm^{-1} is assigned to PyH* [39]. By contrast, for Cu-bpy, in addition to the peaks of PyH* and Py, an interface water peak can also be observed at 1654 cm^{-1} (Fig. 4b), similar to those of CuCl, Cu-dpb and Cu-bpe (Fig. S24). In the Cu-bpa spectra, we can observe the downward and upward Py peaks at 1613 and 1431 cm^{-1}, respectively, suggesting that the conversion reaction between PyH* and Py is reversible. The proton resulting from the deprotonation of PyH* promotes the hydrogenation of *CO intermediates. Therefore, the proton source for CH_4 formation is PyH* (Fig. 4c). In the Cu-bpy spectra, we can observe the upward Py peaks at 1431 cm^{-1} and not observe downward Py peak at 1614 cm^{-1}, suggesting that the deprotonation of PyH* is hardly carried out with the formation of Py. It results in a slow proton transfer, which promotes *CO dimerization. Thereby, the proton source for C_2H_4 formation is water (Fig. 4d). In addition, the interface water peak of Cu-bpy indicates the formation of a strong hydrogen bonding [40]. The previous report has demonstrated that the hydrogen bonding can stabilize *CO intermediates and increase its coverage, thereby enhancing the dimerization for C_2H_4 formation [41], which agrees well with our electrochemical observations.

Structure-property relationship of molecular electrophilicity and CRR selectivity

We then investigated the critical intermediates in CRR to understand the influence of catalysts' proton availability on the PCET processes. A CHO* intermediate at 1505 cm^{-1} is clearly observed on Cu-bpa with potential being applied (Fig. 5a). This intermediate can achieve further hydrogenation *via* a series of

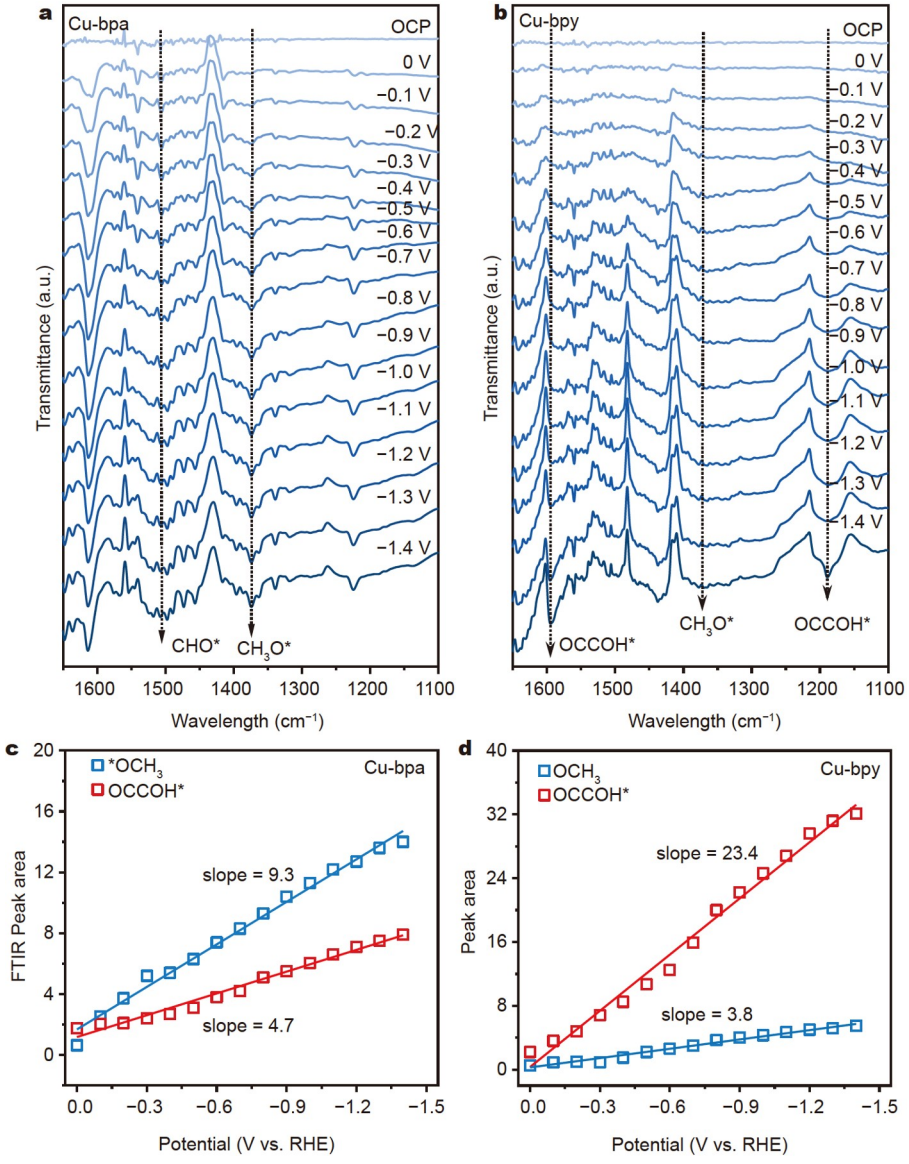

Figure 5 (a, b) *In situ* ATR-IR spectra on Cu-bpa and Cu-bpy at different potentials of CRR. All potentials are *versus* RHE. (c, d) Integrated peak area of *OCH_3 and OCCOH* on Cu-bpa and Cu-bpy under different potentials.

PCET reactions to form *OCH_3, which is the final intermediate in the generation of CH_4 [42]. By contrast, Cu-bpy exhibits two strong peaks at 1595 and 1190 cm^{-1} (Fig. 5b), which correspond to OCCOH* for the formation of C_2H_4. This is derived from the dimerization of two *CO and then further hydrogenation [43]. The linear relationships between the integral area of these two intermediates and potentials show that the slope of *OCH_3 is nearly twice that of OCCOH* on Cu-bpa, whereas the slope of *OCH_3 is one-sixth that of OCCOH* on Cu-bpy (Fig. 5c, d, and Fig. S25). By contrast, a lower slope of OCCOH* was observed on Cu-dpb, whereas a higher slope of OCCOH* was also observed on Cu-bpe (Fig. S26).

We further compared the slope ratio of OCCOH* to *OCH_3 for Cu-bpa, Cu-dpb, Cu-bpy, and Cu-bpe. It increases from 0.5 to 5.7, 6.2 and 12.2, respectively, with the increase of linker electrophilicity. This result suggests that the linker with a higher electrophilicity favors the formation of OCCOH* while inhibits that of *OCH_3. Therefore, this trend clearly explains the intrinsic reason that Cu-bpa generates CH_4 as the dominant product while Cu-bpe produces C_2H_4, matching well with the CRR results.

CONCLUSION

In summary, we developed a molecular engineering strategy to regulate CRR selectivity of CH_4 and C_2H_4 on MOF-derived-Cu catalysts. Based on the DFT computation, electrochemical results, *in situ* ATR-IR as well as Raman spectroscopy analysis, we explicitly revealed the regulation mechanism by tuning the molecular electrophilicity and proton availability to alter the critical PCET processes in CRR. We found that the linker with low electrophilicity can promote proton transfer from PyH* to *CO intermediates, thus facilitating the formation of CH_4. By contrast, the linker with high electrophilicity can build strong hydrogen bond to stabilize the *CO dimer, thereby favoring the C_2H_4 formation. This finding provides new insights into steering CRR selectivity on Cu-based catalysts by tuning the PCET process, which could also guide the catalyst design for other proton-involving electrochemical reactions.

Received 10 October 2023; accepted 31 October 2023; published online 26 December 2023

1 Wang G, Chen J, Ding Y, *et al.* Electrocatalysis for CO_2 conversion: From fundamentals to value-added products. Chem Soc Rev, 2021, 50: 4993–5061
2 Lv JJ, Yin R, Zhou L, *et al.* Microenvironment engineering for the electrocatalytic CO_2 reduction reaction. Angew Chem Int Ed, 2022, 61: e202207252
3 Zhang W, Jin Z, Chen Z. Rational-designed principles for electrochemical and photoelectrochemical upgrading of CO_2 to value-added chemicals. Adv Sci, 2022, 9: e2105204
4 Liu M, Pang Y, Zhang B, *et al.* Enhanced electrocatalytic CO_2 reduction *via* field-induced reagent concentration. Nature, 2016, 537: 382–386
5 Tabassum H, Yang X, Zou R, *et al.* Surface engineering of Cu catalysts for electrochemical reduction of CO_2 to value-added multi-carbon products. Chem Catal, 2022, 2: 1561–1593
6 Nitopi S, Bertheussen E, Scott SB, *et al.* Progress and perspectives of electrochemical CO_2 reduction on copper in aqueous electrolyte. Chem Rev, 2019, 119: 7610–7672
7 Zi X, Zhou Y, Zhu L, *et al.* Breaking K^+ concentration limit on Cu nanoneedles for acidic electrocatalytic CO_2 reduction to multi-carbon products. Angew Chem Int Ed, 2023, 62: e202309351
8 Yang B, Liu K, Li HJW, *et al.* Accelerating CO_2 electroreduction to multicarbon products *via* synergistic electric–thermal field on copper nanoneedles. J Am Chem Soc, 2022, 144: 3039–3049
9 Zhou Y, Liang Y, Fu J, *et al.* Vertical Cu nanoneedle arrays enhance the local electric field promoting C_2 hydrocarbons in the CO_2 electroreduction. Nano Lett, 2022, 22: 1963–1970
10 Lee CW, Yang KD, Nam DH, *et al.* Defining a materials database for the design of copper binary alloy catalysts for electrochemical CO_2 conversion. Adv Mater, 2018, 30: e1704717
11 Yang PP, Zhang XL, Gao FY, *et al.* Protecting copper oxidation state *via* intermediate confinement for selective CO_2 electroreduction to C_{2+} fuels. J Am Chem Soc, 2020, 142: 6400–6408
12 Wakerley D, Lamaison S, Ozanam F, *et al.* Bio-inspired hydrophobicity promotes CO_2 reduction on a Cu surface. Nat Mater, 2019, 18: 1222–1227
13 Zhou X, Liu H, Xia BY, *et al.* Customizing the microenvironment of CO_2 electrocatalysis *via* three-phase interface engineering. SmartMat, 2022, 3: 111–129
14 Xue W, Liu H, Chen X, *et al. Operando* reconstruction towards stable CuI nanodots with favorable facets for selective CO_2 electroreduction to C_2H_4. Sci China Chem, 2023, 66: 1834–1843
15 Zhao X, Du L, You B, *et al.* Integrated design for electrocatalytic carbon dioxide reduction. Catal Sci Technol, 2020, 10: 2711–2720
16 Jiang N, Zhu Z, Xue W, *et al.* Emerging electrocatalysts for water oxidation under near-neutral CO_2 reduction conditions. Adv Mater, 2022, 34: e2105852
17 Ma W, Xie S, Liu T, *et al.* Electrocatalytic reduction of CO_2 to ethylene and ethanol through hydrogen-assisted C–C coupling over fluorine-modified copper. Nat Catal, 2020, 3: 478–487
18 Wang X, Ou P, Wicks J, *et al.* Gold-in-copper at low *CO coverage enables efficient electromethanation of CO_2. Nat Commun, 2021, 12: 3387
19 Zheng Y, Vasileff A, Zhou X, *et al.* Understanding the roadmap for electrochemical reduction of CO_2 to multi-carbon oxygenates and hydrocarbons on copper-based catalysts. J Am Chem Soc, 2019, 141: 7646–7659
20 Zhao J, Zhang P, Yuan T, *et al.* Modulation of *CH_xO adsorption to facilitate electrocatalytic reduction of CO_2 to CH_4 over Cu-based catalysts. J Am Chem Soc, 2023, 145: 6622–6627
21 Zhao Y, Zu X, Chen R, *et al.* Industrial-current-density CO_2-to-C_{2+} electroreduction by anti-swelling anion-exchange ionomer-modified oxide-derived Cu nanosheets. J Am Chem Soc, 2022, 144: 10446–10454
22 Li F, Thevenon A, Rosas-Hernández A, *et al.* Molecular tuning of CO_2-to-ethylene conversion. Nature, 2020, 577: 509–513
23 Chen S, Zhang Z, Jiang W, *et al.* Engineering water molecules activation center on multisite electrocatalysts for enhanced CO_2 methanation. J Am Chem Soc, 2022, 144: 12807–12815
24 Dey S, Masero F, Brack E, *et al.* Electrocatalytic metal hydride generation using CPET mediators. Nature, 2022, 607: 499–506
25 Agarwal RG, Coste SC, Groff BD, *et al.* Free energies of proton-coupled electron transfer reagents and their applications. Chem Rev, 2022, 122: 1–49doi: 10.1021/acs.chemrev.1c00521
26 Zhou X, Jin H, Xia BY, *et al.* Molecular cleavage of metal-organic frameworks and application to energy storage and conversion. Adv Mater, 2021, 33: 2104341
27 Zhang W, Liu S, Yang Y, *et al.* Exclusive Co-N_4 sites confined in two-dimensional metal-organic layers enabling highly selective CO_2 electroreduction at industrial-level current. Angew Chem Int Ed, 2023, 62: e202219241
28 Vasileff A, Xu C, Jiao Y, *et al.* Surface and interface engineering in copper-based bimetallic materials for selective CO_2 electroreduction. Chem, 2018, 4: 1809–1831
29 Li T, Jing Y. Band structure engineering of 2D heterotriangulene polymers by incorporating acetylenic linkages for photocatalytic hydrogen production. J Phys Chem C, 2022, 126: 17836–17843
30 Yaghi OM, Li G. Mutually interpenetrating sheets and channels in the extended structure of [Cu(4,4′-bpy)Cl]. Angew Chem Int Ed Engl, 1995, 34: 207–209
31 Sprague-Klein EA, Ho-Wu R, Nguyen D, *et al.* Modulating the electron affinity of small bipyridyl molecules on single gold nanoparticles for plasmon-driven electron transfer. J Phys Chem C, 2021, 125: 22142–

22153
32 Uchida T, Mogami H, Yamakata A, *et al.* Hydrogen evolution reaction catalyzed by proton-coupled redox cycle of 4,4′-bipyridine monolayer adsorbed on silver electrodes. J Am Chem Soc, 2008, 130: 10862–10863
33 Ertem MZ, Konezny SJ, Araujo CM, *et al.* Functional role of pyridinium during aqueous electrochemical reduction of CO_2 on Pt(111). J Phys Chem Lett, 2013, 4: 745–748
34 Ahmed A, Robertson CM, Steiner A, *et al.* $Cu^{(I)}Cu^{(II)}$BTC, a microporous mixed-valence MOF *via* reduction of HKUST-1. RSC Adv, 2016, 6: 8902–8905
35 Zhou X, Dong J, Zhu Y, *et al.* Molecular scalpel to chemically cleave metal-organic frameworks for induced phase transition. J Am Chem Soc, 2021, 143: 6681–6690
36 Zheng M, Wang P, Zhi X, *et al.* Electrocatalytic CO_2-to-C_{2+} with ampere-level current on heteroatom-engineered copper *via* tuning *CO intermediate coverage. J Am Chem Soc, 2022, 144: 14936–14944
37 Zhang XD, Liu T, Liu C, *et al.* Asymmetric low-frequency pulsed strategy enables ultralong CO_2 reduction stability and controllable product selectivity. J Am Chem Soc, 2023, 145: 2195–2206
38 Wu ZZ, Zhang XL, Niu ZZ, *et al.* Identification of Cu(100)/Cu(111) interfaces as superior active sites for CO dimerization during CO_2 electroreduction. J Am Chem Soc, 2022, 144: 259–269
39 Dunwell M, Yan Y, Xu B. *In situ* infrared spectroscopic investigations of pyridine-mediated CO_2 reduction on Pt electrocatalysts. ACS Catal, 2017, 7: 5410–5419
40 Ataka K, Yotsuyanagi T, Osawa M. Potential-dependent reorientation of water molecules at an electrode/electrolyte interface studied by surface-enhanced infrared absorption spectroscopy. J Phys Chem, 1996, 100: 10664–10672
41 Ahn S, Klyukin K, Wakeham RJ, *et al.* Poly-amide modified copper foam electrodes for enhanced electrochemical reduction of carbon dioxide. ACS Catal, 2018, 8: 4132–4142
42 Zhou X, Shan J, Chen L, *et al.* Stabilizing Cu^{2+} ions by solid solutions to promote CO_2 electroreduction to methane. J Am Chem Soc, 2022, 144: 2079–2084
43 Pérez-Gallent E, Figueiredo MC, Calle-Vallejo F, *et al.* Spectroscopic observation of a hydrogenated CO dimer intermediate during CO reduction on Cu(100) electrodes. Angew Chem Int Ed, 2017, 56: 3621–3624

Acknowledgements This work was supported by the Australian Research Council through the Discovery Project programs (FL170100154, FT200100062, DP220102596 and DP190103472). DFT computations were undertaken with the assistance of resources and services from the National Computational Infrastructure (NCI). The hard X-ray adsorption measurements were carried out at Taiwan Photon Source (TPS), Synchrotron Radiation Research Center. Zhou X acknowledges the support from the Australian Government through the Research Training Program Scholarships.

Author contributions Zhou X, Zheng Y, and Xia BY conceived the project and designed the experiments. Zhou X performed the experiments. Shan J and Zheng M carried out the *in situ* characterizations. Li H conducted the DFT calculations. All authors discussed the results and commented on the manuscript.

Conflict of interest The authors declare that they have no conflict of interest.

Supplementary information Experimental details and supporting data are available in the online version of the paper.

Xianlong Zhou received his ME degree from Nankai University (China) and PhD degree under the supervision of Assoc. Prof. Yao Zheng and Prof. Shi-Zhang Qiao at the School of Chemical Engineering and Advanced Materials, The University of Adelaide. Now, he works at Nanjing Forestry University and his research focuses on electrochemical reduction of CO_2.

Yao Zheng received his PhD degree in 2014 from the University of Queensland (Australia). He is currently a Professor at The University of Adelaide. His current research focuses on fundamental studies of some key electrocatalysis processes by combining experiments and theoretical computations, and the development of advanced electrocatalysts for electrocatalytic refinery processes.

调节铜催化剂表面分子亲电性以调控电催化二氧化碳还原选择性

周贤龙[1,3†], 单洁琼[1†], 郑敏[1†], 李欢[1], 夏宝玉[2*], 郑尧[1*]

摘要 Cu是唯一能选择性将二氧化碳电还原(CRR)为多碳产物的过渡金属. 然而, 调控Cu的CRR选择性获得多种产物仍非常具有挑战性. 本文选择了一系列具有不同亲电性的分子来修饰Cu催化剂以调控其CRR选择性, 从而产生CH_4或C_2H_4. 理论计算表明, 分子的亲电性决定催化反应中的质子活度, 进而能促进或抑制CRR中的质子耦合电子转移(PCET)过程. 实验发现, 低亲电性分子(如1,2-双(4-吡啶基)乙烷)可以促进质子转移, 加快*CO中间体氢化过程而生成CH_4, 实现58.2%的法拉第效率; 而高亲电性分子(如顺-1,2-双(4-吡啶基)乙烯)能构建强的氢键以稳定*CO中间体, 促进其偶联生成C_2H_4, 实现65.9%的法拉第效率. 理论计算结合原位光谱表征揭示, 分子亲电性可调节催化剂质子活度, 影响CRR反应中*CO氢化或偶联, 进而调控CRR选择性. 不同于常规的催化剂结构工程, 本策略通过调节CRR中的PCET过程来调控选择性, 为CRR的发展提供了新的认识.